



Sustainable Energy and Fuels

ARTICLE

Hydrogen production by ethanol steam reforming on Ni-based catalysts: effect of the support and of CaO and Au doping

Received 00th January 20xx,
Accepted 00th January 20xx

DOI: 10.1039/x0xx00000x
www.rsc.org/

Federica Menegazzo^a, Cristina Pizzolitto^a, Danny Zanardo^a, Michela Signoretto^{a*}, Cas Buyschaert^b, Guido Bény^b and Alessandro Di Michele^c

Nickel-based catalysts were investigated for hydrogen production by ethanol steam reforming. A suitable support was looked for among the metal oxides TiO₂, ZrO₂ and CeO₂. Alongside catalytic testing with ethanol-water mixture, a series of characterization measurements were carried out: N₂-physisorption, XRD, TPR, TPO, CO₂-TPD, SEM, AAS and IC. Zirconium and cerium oxides proved to be suitable supports, even if both still suffer from coking phenomena. The effects of doping by both calcium oxide and gold nanoparticles were checked. Doping by calcium oxide prevented deactivation and highly increased the hydrogen yield. Moreover, the addition of gold nanoparticles greatly improved the hydrogen yield. The combination of the two dopants resulted in the best performing catalyst: the basic doping by CaO and the promotion of the water gas shift reaction by gold nanoparticles contributed to the highest hydrogen production.

1. Introduction

Energy is the base for social and economic development, and it represents a necessity for everyday life. There are estimations that the energy consumption will continuously increase doubling its value from 2009 to 2050.¹ More than 80% of all energy is produced from fossil fuels respectively oil, coal and gas. In the BP report, about the future of energy in 2016 a decrease in the use of oil and coal is predicted in the next 20 years.² A high usage of fossil fuels means a high production of greenhouse gases, which is causing the global warming phenomenon. For every carbon atom used, a carbon dioxide molecule (in optimal condition) or a carbon monoxide molecule (in non-optimal conditions) is emitted in the atmosphere. Another problem humanity has been stumbling on is the fast depletion of the reserves of these fossil fuels, even if new drilling, new oil fields and extraction technologies are continuously developing. To lower the consumption of fossil fuels and thus the production of greenhouses there are several strategies. One of them is the use of clean and renewable energy resources instead of fossil fuels, which provides an additional solution. Some examples of renewables are wind power, hydropower, solar energy and geothermal energy. These are all endless, so sustainable from an economic and environmental point of view but not storable.³ Research

showed hydrogen as a suitable candidate to solve both these problems, cleanliness and storage problem. Storing a gas is not a new technology and the compressed gas is already in use in the vehicle industry.⁴ In addition, hydrogen is considered a fuel source due to the clean combustion reaction, which produces only water as by-product. More interestingly, hydrogen fuel cells are commonly used in the transportation sector due to the ability to convert chemical energy into electricity. However, the use of hydrogen as energy vector is not limited to the transport industry. The size flexibility of the fuel cells may be the biggest strength of hydrogen power. The potential ranges from a few watt application to megawatt structures. A third possible use of the fuel cells are in combined heat and power systems for buildings.

Actually, the other problem, the fossil fuel consumption, is still present because hydrogen is mainly produced from fossil fuels. The use of hydrogen will be completely renewable when it will be produced using a sustainable resource. A possible process to produce hydrogen is ethanol steam reforming (ESR). Nowadays ethanol is already mostly produced from biomass therefore from an infinite and renewable source.⁵ The ESR is a complex process where different pathways can be pursued, as reported in Figure 1. The pathway that is the most important is the direct steam reforming of ethanol (1). Compared to the other pathways, this reaction path has the highest yield in terms of hydrogen formation, since it supplies six hydrogen molecules per ethanol molecule. The other important reaction that should be promoted is the water-gas shift reaction (WGS) of the intermediate CO (10), which further increases the hydrogen yield. Other reactions can occur simultaneously but are not desirable. The dehydration of ethanol (2) is the least wanted reaction, no hydrogen is produced and there is a chance the

^a CATMAT Lab, Department of Molecular Sciences and Nanosystems, Ca' Foscari University Venice and INSTM-RU Ve, Via Torino 155, 30172 Venezia Mestre, Italy; *miky@unive.it

^b KU Leuven, Chemical Engineering, Faculty of Engineering Technology, Campus Group T Leuven, Vesaliusstraat 13, 3000 Leuven, Belgium

^c Physics and Geology Department, University of Perugia, Via Pascoli, 06123 Perugia, Italy

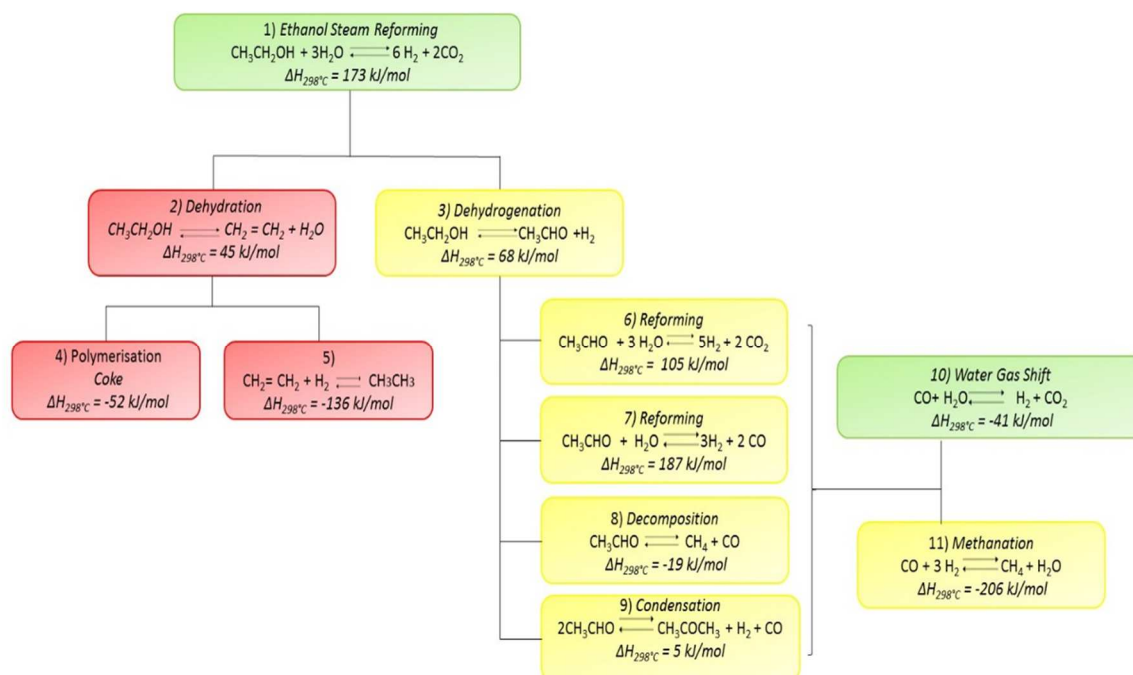
formed ethylene is polymerized to coke (4). Designing the proper catalyst is able to favour only specific reactions or to prevent others from happening. The catalytic system for the direct ESR should be developed in order to break C-C bonds whereas the WGS reaction should be promoted in order to prevent CO production and coke deposition. Choosing a correct support is a matter of vital importance to obtain an active, thermally stable catalyst, which is not deactivated in a certain time of reaction. Essential characteristics for a support are its stability in the reaction media, a low cost, adequate porous structure and high surface area to allow a high dispersion of the active phase. Another important property is the acidity of the support. A basic support is more resistant to coke deposition while acidic ones are promoting the formation of carbon containing species on the catalytic surface. In fact, it is well known that the side reactions leading to the formation of coke occur mainly on the acid sites of the support.⁶⁻⁹ This means that the support plays a key role in determining the reaction pathway and, as a consequence, the selectivity of the process.¹⁰ For example, Al₂O₃ promotes the dehydration of ethanol to ethylene¹¹⁻¹³ and the dehydration is likely to end up with coke formation.

As the choice of the support plays a vital role in determining the activity, selectivity and stability of a catalyst, three different metal oxides were investigated. In particular, it was chosen

TiO₂, as it is inexpensive and has high chemical stability; ZrO₂, for its thermal and chemical stability; CeO₂, because it has a high ability to store and deliver oxygen¹⁴⁻¹⁶, due to its ability to change the oxidation state from +3 to +4.¹⁷ The oxygen that is available on the surface can limit the deposition of carbon containing compounds through coke gasification with a consequent increase in the catalytic performance of the system.^{18, 19} Moreover, it was proved that cerium oxide minimizes the thermal impact on the metallic phase and increases the stability due to the strong interaction of ceria with the metal particles.

As regard to the active phase, a non-noble metal is extremely attractive to upscale the process for one reason: the price. In comparison with other metals used in these systems, like platinum and rhodium, nickel cost is extremely reduced. Nickel showed a high activity and efficiency in breaking the C-C bond. Actually the use of nickel is limited by coking and Ni sintering phenomena.^{20, 21} Noble metals are known for their ability to break the C-C bond and it's known that gold nanoparticles favour the water gas-shift reaction as well.²²⁻²⁴ However, the particle size of the gold nanoparticles is of great importance for the catalytic activity and inhibiting the sintering of the nanoparticles is crucial in terms of the long-term activity.²⁵

Figure 1: Possible reaction pathways for catalytic ethanol steam reforming



Bimetallic catalysts could provide a positive synergistic effect due to both metals. Studies reported the effect of combining gold with other metals that are active for the water-gas shift reaction.^{26, 27} Nickel in combination with gold on Fe₂O₃ support showed an increase of the rate at higher temperatures for CO-PROX reaction.²³ For low temperature methane steam reforming it was found that, compared to monometallic Ni catalysts, Ni-Au bimetallic catalysts exhibit superior catalytic performance, i.e., high activity, high resistance to carbon formation and sintering of metal particles, and high selectivity to H₂ product. Such improvement was ascribed to the synergic effect between a second metal and Ni by the formation of a superficial bimetallic alloy.²⁰ As regard to ESR, a recent study²⁸ shows interesting results with Ni-Au/SBA-15 catalysts: it was found that the addition of Au promoter improved both catalytic activity and stability. In particular, the addition of Au strengthened the interaction between the SBA-15 support and NiO/Ni phase to form well-dispersed, small nickel particles. These promoting effects of Au not only prevented the active nickel particle from sintering, but also suppressed the carbon deposition over the active nickel particles. Therefore, it should be much interesting to investigate the effect of gold addition to nickel for ESR for three much more common supports than SBA-15, such as titania, zirconia and ceria. Moreover, calcium oxide was added to the supports in order to reduce the acidity of the catalysts and prevent coke formation.

The aim of the present work is the development of Ni based catalysts supported on titania, zirconia and ceria for hydrogen production by ESR. In particular, the addition of calcium oxide by incipient wetness impregnation and of a small amount of gold by deposition precipitation were investigated. Samples were properly characterized to understand the influence of the dopants on morphological, textural and surface properties. The evaluation of the catalytic performances in the ESR were proved in a plug-flow reactor.

2. Experimental

2.1 Synthesis of supports

Titanium hydroxide was precipitated at pH=8.6 by the drop wise addition of 9 M ammonia solution to a 0.5 M TiOSO₄·xH₂SO₄·yH₂O (Aldrich) aqueous solution. After aging at 60 °C for 20 hours, the precipitate was filtered, washed with distilled water in order to remove SO₄²⁻ ions and dried at 110 °C for 18 hours. The absence of sulphates in the material was verified by IC analysis. Finally, the hydroxide was calcined in flowing air (30 mL/min) at 500 °C for 3 hours.²⁹

Zirconium hydroxide was prepared by precipitation from ZrOCl₂·8H₂O (Aldrich) at constant pH= 8.6 and then aged for 20 hours at 90 °C.²¹ Then Zr(OH)₄ was calcined in flowing air (30 mL/min) at 650 °C for 3 hours.

Ceria support was synthesized by precipitation from (NH₄)₂Ce(NO₃)₆ (Aldrich) by urea at 100 °C in aqueous solution.³⁰ The solution was mixed and boiled for 6 h at 100 °C, the precipitate was washed in boiling deionized water and dried at 110 °C for 18 hours. The material was then calcined in flowing air (30 mL/min) at 650 °C for 3 hours.

2.2 Synthesis of catalysts

The metal introduction on the support was performed by incipient wetness impregnation with a proper amount of nickel nitrate aqueous solution in order to obtain 10 wt% of nickel on the material. After drying in an oven at 110 °C for 15 hours, a calcination was performed in flowing air (30 mL/min) at 500 °C for 4 hours.

Calcium was added by incipient wetness impregnation from a proper amount of calcium nitrate in order to obtain 9 wt % of CaO on the support.

Gold was added by deposition-precipitation method.²² A proper amount of HAuCl₄ was solved in 200 ml of distilled water at 60 °C. After adding 0.5M NaOH to a pH of 8.6, the support with nickel or nickel and calcium is added and stirred for 3 hours. The catalyst was then filtered, washed, dried at 110 °C for 18 hours and finally calcined in flowing air (30 mL/min) at 500 °C for 4 hours.

The samples will be referred to as:

| | |
|-----------|--|
| Ni-Ti | 10 wt%Ni/TiO ₂ |
| Ni-Zr | 10 wt%Ni/ZrO ₂ |
| Ni-Ce | 10 wt%Ni/CeO ₂ |
| CaNi-Zr | 10 wt%Ni/9 wt%CaO/ZrO ₂ |
| CaNi-Ce | 10 wt%Ni/9 wt%CaO/CeO ₂ |
| AuNi-Ce | 10 wt%Ni/1 wt%Au/CeO ₂ |
| AuCaNi-Ce | 10 wt%Ni/9 wt%CaO/1 wt%Au/CeO ₂ |

2.3 Methods

Surface areas and pore size distributions were obtained from N₂ adsorption/desorption isotherms at -196 °C using a Micromeritics ASAP 2000 analyser. Surface area was calculated from the N₂ adsorption isotherm by the BET equation³¹, and pore size distribution was determined by the BJH method.³²

Temperature programmed reductions (TPR) were carried out in a lab-made equipment: samples (100 mg) were heated with a temperature rate of 10 °C/min from 25 °C to 900 °C in a 5 %H₂/Ar flow (40 mL/min). The effluent gases were analysed by a TCD detector and by a Genesys 422 quadrupole mass analyzer (QMS).

Temperature programmed desorption of CO₂ (CO₂-TPD) were carried out in the same lab-made equipment used for TPR. 100 mg of sample were exposed to a CO₂ flow at room temperature and then were heated with a temperature rate of 10 °C/min from 25 °C to 800 °C in He flow.

After the reaction, a temperature programmed oxidation (TPO) was carried out. The used catalysts (100 mg) were heated with a temperature rate of 10 °C/min from 25 °C to 800 °C in air flow (40 mL/min) and analysed by a Genesys 422 quadrupole mass analyzer (QMS).

The calcium content was determined by ion chromatography (IC). Calcium concentration was calculated as the average of two independent analyses, each including two chromatographic determinations.

Ni and Au amounts were determined by atomic absorption spectroscopy (AAS) after microwave disaggregation of the samples (100 mg) using a Perkin-Elmer Analyst 100.

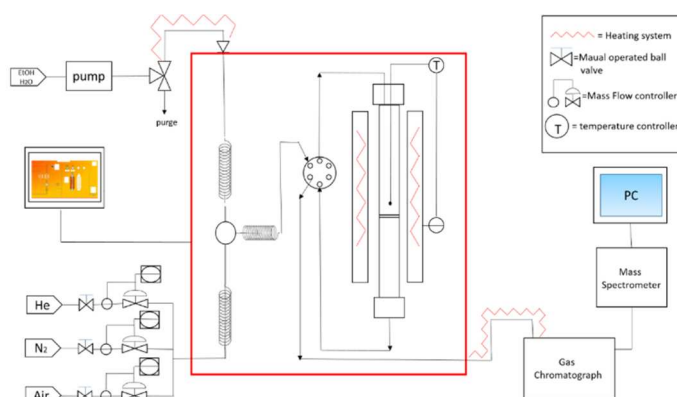
The X-ray diffraction (XRD) data were collected by a Philips X'PERT PRO MPD diffractometer operating at 40 kV and 40 mA, with a step size of 0.0170 2θ degree and step scan of 20 s, using Cu Kα radiation.

SEM images were obtained using Field Emission Gun Electron Scanning Microscopy LEO 1525 ZEISS, after metallization with chromium. The images were acquired by Inlens detector while elemental composition was determined using Bruker Quantax EDS.

2.4 Catalytic test

The catalytic tests were performed with a reference reactor PID (Process Integral Development Eng &Tech) coupled to a gas-chromatograph (HP 6890) and to a Genesys 422 quadrupole mass analyzer (QMS). A schematization is shown in Figure 2. Microactivity-Effi reactor is an automatic computerized high-pressure catalytic reactor which includes valves and process layout inside a hot box to avoid possible condensation of volatile products, and to preheat, at the same time, the reactants efficiently. Using a HPLC pump (Gilson 303) the mixture of water and ethanol (molar ratio 3:1, volume ratio 52%/48%) was flowing with 0,02 mL/min. Helium (230 mL/min) was used as carrier. The typical reaction temperature was 500 °C. Preliminary blank tests showed the absence of conversion at this temperature.

Figure 2: Lab set-up



To have a homogenous catalyst, tablets were pressed and grained to obtain the ideal grain size range (0,3-0,4mm). Afterwards the catalyst was mixed with siliciumcarbide (SiC) with the same grain size. The catalysts were not reduced before reaction.

After the analysis, the following data were calculated:

Conversion of ethanol:

$$\text{conversion (\%)} = [1 - (n_{\text{out EtOH}}) / (n_{\text{in EtOH}})] * 100$$

Carbon balance:

$$\text{carbon balance (\%)} = ((\sum f_i * n_{\text{Ci}}) / (2 * f_{\text{EtOH in}})) * 100$$

Hydrogen yield:

$$\text{yield(H}_2\text{) (\%)} = f(\text{H}_2) / (6 * f_{\text{EtOH in}}) * 100$$

Hydrogen productivity:

$$\text{productivity (H}_2\text{) (mol/(min*kg))} = f(\text{H}_2) / m_{\text{catalyst}}$$

Selectivity:

$$\text{selectivity (\%)} = (f_{i \text{ out}} / (f_{\text{EtOH in}} - f_{\text{EtOH out}})) * 100$$

With n number of moles; f, flux in mL/min; m, mass in kg.

3. Results and discussion

3.1 Effect of the support

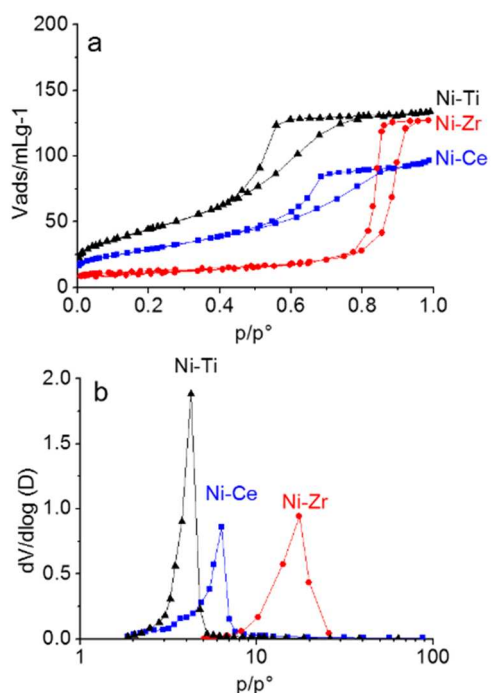
First, nitrogen physisorption analyses were performed in order to provide information about the surface area and the pore size distribution of the catalysts. It can be assumed that they are almost the same to that of the plain supports, because the calcination temperature of the final catalysts is equal to or even lower than supports calcination ones. In Figure 3 N₂ adsorption/desorption isotherms (section a) and corresponding BJH pore size distribution (section b) are shown. All graphs are type IV isotherms with a type H₂ hysteresis loop, according to the IUPAC-classification.

All the samples have a mesoporous structure and a unimodal pore size distribution. The adsorption for Ni-Zr sample is shifted toward higher values, indicating the presence of larger pores than on Ni-Ti and Ni-Ce. Table 1 shows the results of surface area and mean pore size. As regard as surface area, Ni-Zr presents the lowest one (53 m²/g), while Ni-Ti and Ni-Ce have similar values around 100 m²/g. Table 1 reports also the effective amounts of nickel, which is almost the same for all samples (around 8 wt%).

Table 1: Physicochemical properties of the Ni plain samples

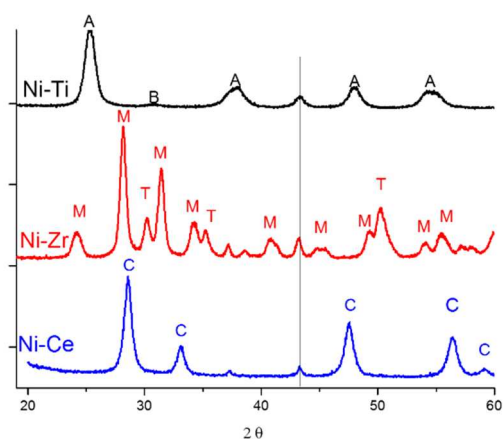
| | Ni-Ti | Ni-Zr | Ni-Ce |
|--------------------------------------|-------|-------|-------|
| BET surface area (m ² /g) | 101 | 53 | 105 |
| Mean pore size (nm) | 4 | 17 | 5 |
| Effective Ni amount (wt%) | 8.0 | 8.2 | 8.5 |

Figure 3: N₂ physisorption isotherms of the catalysts (section a) and their BBJ pore size distributions (section b). Ni-Ti (▲), Ni-Zr (◆), Ni-Ce (■)



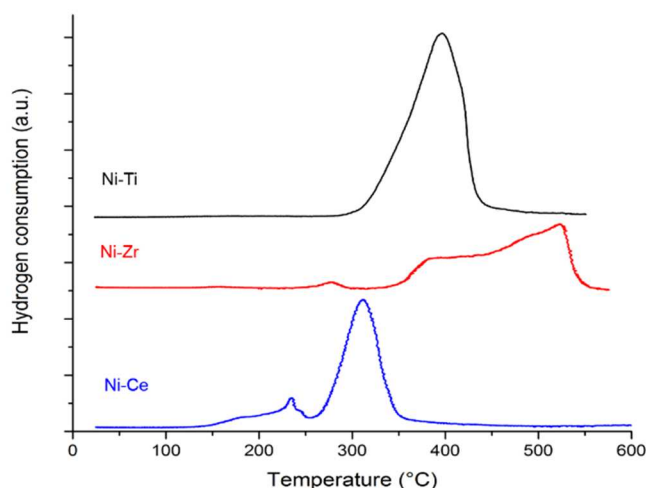
XRD analyses were performed in order to check the phases of the supports and the presence of Ni or NiO peaks. The results are shown in Figure 4. For Ni-Ti, the main phase of the support is nanocrystalline anatase (A) observed at 2θ 25, 38, 48 and 55 °, with a small percentage of brookite (B) observed at 2θ 32 °. In the case of Ni-Zr sample, a tetragonal phase is observed at 2θ 30.2, 35.5 and 50.3 °, while monocline phase is evident for 2θ 24.3, 28.0, 31.55, 34.2, 40.8, 44.9, 45.5, 49.4, 54.0, 55.4. As regard as Ni-Ce, the peaks observed at 2θ 28, 33.2, 47.5, 56, 59 and 69 ° can be assigned to respectively (111), (200), (220), (311), (222) and (400) peaks of cubic CeO₂ (ceria (Ce), syn; file number 00-034-0394). The occurrence of NiO is clearly detected at 2θ 43.4 ° for all the three sample, while there is not evidence for Ni⁰ phase.

Figure 4: XRD analyses of Ni-Ti, Ni-Zr, Ni-Ce.



In order to identify the different NiO species on the surface of the supports and their reduction temperature, programmed temperature reductions (TPR) were carried out (Figure 5). Both the TPR profiles of Ni-Zr and Ni-Ce show a small peak at the beginning of the spectrum, which indicates that a portion of nickel is free NiO, that is Ni non-interacting with the support.^{33, 34} On the contrary, on Ni-Ti sample there is not free NiO, but only one species of Ni interacting with titania and reducible at 400 °C. The TPR profile of Ni-Ce shows that, besides the first low temperature peak, all nickel is of the same species on this support and reducible at 320 °C. The TPR profile of Ni-Zr shows multiple peaks, in a broad region between 350 °C and 550 °C. Each peak is representing a nickel species with different strengths of interaction with the support.^{35, 36} The higher the reduction temperature of a nickel species, the stronger the interaction with the support. In every case, the Ni is reduced at temperature lower than 500 °C, which is the reaction temperature for ESR. This means that probably in all cases the reduced Ni formed with hydrogen production is present during the ESR process.

Figure 5: TPR profiles of Ni-Ti, Ni-Zr and Ni-Ce



The next step was to test in the ESR the samples supported on TiO₂, ZrO₂ and CeO₂ (Table 2). In the first two hours of reaction, the titanium-based catalyst is clearly the worst performing in the conversion of ethanol and in general, it is the least performing sample for hydrogen production.

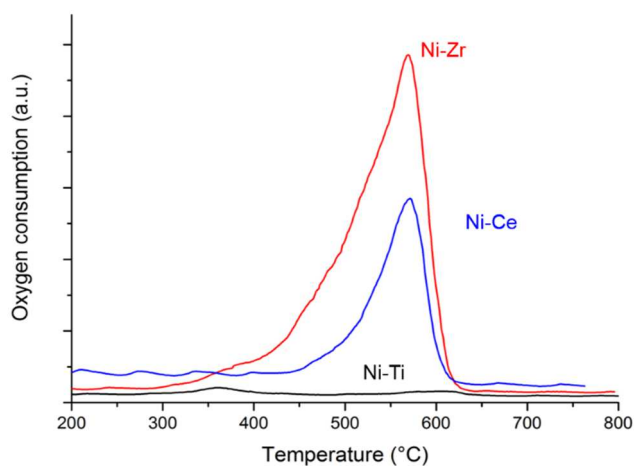
The second striking thing is the stability of the cerium based catalyst in ESR: a total conversion is maintained for more than 10 hours, while using the zirconium-based catalyst, the conversion of ethanol started to decrease after one hour of reaction. The activity loss happened gradually, in contrast to Ni-Ti where the deactivation was extremely rapid. The explanation for the deactivation can be found in the acidity of the ZrO₂ support, which activates the coke formation.

Table 2: Catalytic performances for Ni-Ti, Ni-Zr and Ni-Ce catalysts

| | After 1 h | | | After 10 h | | |
|---|-----------|-------|-------|------------|-------|-------|
| | Ni-Ti | Ni-Zr | Ni-Ce | Ni-Ti | Ni-Zr | Ni-Ce |
| Ethanol conversion (%) | 10 | 100 | 100 | 0 | 80 | 100 |
| Carbon balance (%) | 90 | 40 | 45 | 100 | 50 | 50 |
| H ₂ yield (%) | 4 | 54 | 50 | 0 | 42 | 50 |
| H ₂ productivity (mol/minKg _{cat}) | 0.1 | 2.0 | 1.8 | 0 | 1.6 | 1.8 |
| CO ₂ (%)–CO (%) | 2-0 | 37-5 | 32-5 | 0-0 | 30-5 | 32-5 |

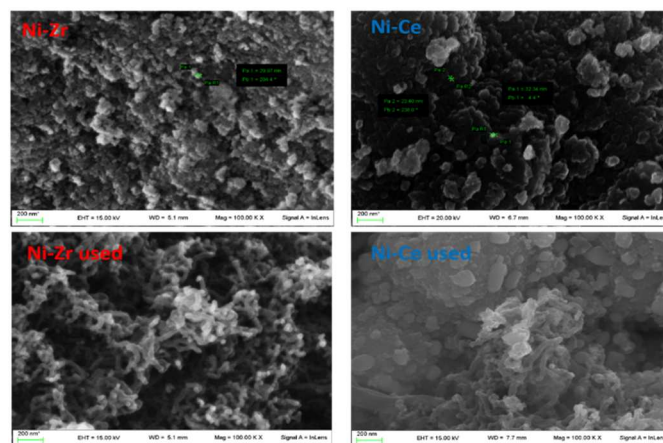
Table 2 shows a high carbon balance for Ni-Ti, the value is almost 100% but it is not significant because it is due to the negligible conversion. Nevertheless, for the two other supports, coke deposition is evident in the calculated carbon balance: the absence of carbon atoms at the outlet means that a large amount of carbon is restrained in the reactor. Coke blocks the catalytic surface where reactions could take place, affecting ethanol conversion in the long term. Another feature both Ni-Zr and Ni-Ce have in common is the selectivity for CO₂ and CO (Table 2), showing that almost no CO is produced.

The hypothesis for coke formation on both catalysts is supported by the TPO measurements on used samples shown in Figure 6.

Figure 6: TPO profiles of Ni-Ti, Ni-Zr and Ni-Ce

The non-reactivity of Ni-Ti can be explained by this technique as well: the TPO profile of the used Ni-Ti does not show any trace of coke formation, due to the low conversion of ethanol. Both Ni-Zr and Ni-Ce display the accumulation of coke. The latter is formed by the dehydration of ethylene. Ethylene is able to polymerize at low temperatures if the conditions are not optimal for the gasification. Carbon polymers on the catalytic surface may lead to deactivation. The fact that the peaks of Ni-Zr and Ni-Ce occur at the same oxidation temperature, means

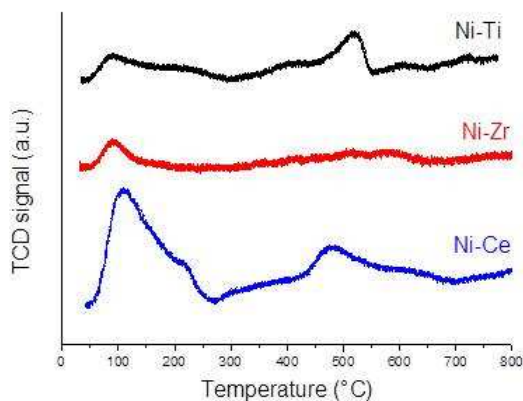
that the kind of coke is similar for both samples. At the same time, Ni-Ce catalyst is less deactivated than Ni-Zr one because its surface is less covered by coke. This fact is confirmed by SEM analysis. Figure 7 presents SEM images of fresh and used catalysts. Looking at the used one, it is noticeable that the all surface of Ni-Zr sample is covered by coke nanotubes. On the contrary, on used Ni-Ce sample, only limited regions are enclosed by coke. The difference between the two materials be found in the acidity of the support. The higher the basicity of the catalyst, the better is the resistance against coke deposition.

Figure 7: SEM analyses of Ni-Zr (fresh and used) and Ni-Ce (fresh and used)

Using TPD technique, with CO₂ as probe molecule, it is possible to investigate the kind of basic sites on the samples and their strength. Results are reported in Figure 8. Ni-Ti and Ni-Ce catalysts showed multiple peaks, associated with the presence of basic sites with different strength. Ni-Ce sample has an intense peak between 50 °C and 250 °C and a broad peak from 300 °C to 800 °C centred at 480 °C. Ni-Ti sample has the same peaks of Ni-Ce but of lower intensity. For Ni-Zr catalyst is possible to perceive only a small peak at 100 °C that can be associated with the CO₂ only physical absorbed with the support. This technique confirms that Ni-Zr catalyst shows very low basic properties, proving that acidity is the source of

deactivation for this catalyst. Nevertheless, even in the case of Ni-Ce, the support CeO₂ does not provide enough basicity to prevent coke formation.

Figure 8: CO₂-TPD profiles of Ni-Ti, Ni-Zr and Ni-Ce catalysts



3.2 Doping with Calcium

In the following sections on catalyst upgrade, only the two better performing supports will be taken into account: zirconium oxide and cerium oxide. With the goal of increasing hydrogen yield of both supports by reducing the deactivation by coke, we have tried to increase their basicity by CaO addition. Figure 9 reports the TPR profiles of CaO doped samples. For CaNi-Ce there is only one sharp peak, which suggests that the effect of nickel and calcium on ceria is combined at these temperatures. However, such peak is shifted to a higher temperature (400 °C) with respect to the TPR of Ni-Ce catalyst (320 °C). Such shift to the right is an indication for the stronger interaction of nickel with the ceria support after the addition of calcium. In the meanwhile, for CaNi-Zr the broad peak is shifted to the left. According to the literature, an increased Ni reducibility in doped samples can be ascribed to the formation of oxygen vacancies, which favor NiO reduction by weakening the Ni-O bond. These oxygen vacancies arise from the replacement of the Zr⁴⁺ cation with one with a lower positive charge (i.e. Ca²⁺).³⁷

Figure 9: TPR profiles of CaNi-Zr and CaNi-Ce

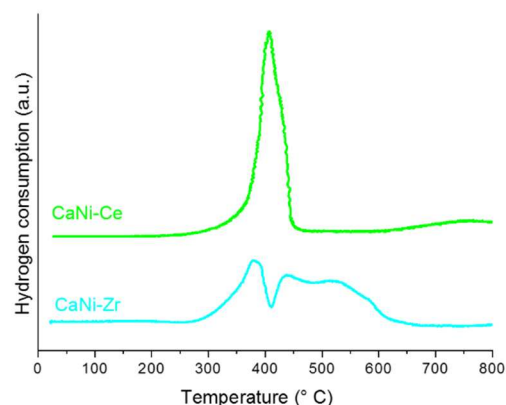


Table 3 shows the differences between CaNi-Zr and CaNi-Ce over several parameters. Also with the addition of CaO, sample on ceria is converting ethanol completely over ten hours, while that on zirconium undergoes a minimal deactivation to 94% conversion. The rate of deactivation is smaller with the addition of calcium, even if it cannot be totally prevented. In terms of hydrogen production, both CaNi-Zr and CaNi-Ce achieve higher yields than Ni-Zr and Ni-Ce. The yield of the zirconium based catalyst increases with over 20% at the 1h and 10h mark, but still deactivation occurs. This can be attributed to the not sufficient effect of the basic power of CaO. Looking at CaNi-Ce, the yield at the 1h mark is 20% higher than for Ni-Ce, while the yield after 10h remains the same for both Ni-Ce and CaNi-Ce. The addition of calcium oxide in this case only positively affects the first 10 hours of the reaction. Unfortunately, deactivation continues to take place, even for the CeO₂ catalyst. The same is valid for the hydrogen productivity, and with the addition of calcium the productivity per kilogram catalyst is remarkably higher. The deactivation of both catalysts can again be ascribed to coke formation.

Table 3. Results of CaNi-Zr and CaNi-Ce samples.

| | CaNi-Zr | | CaNi-Ce | |
|--|-----------|------------|-----------|------------|
| | After 1 h | After 10 h | After 1 h | After 10 h |
| Effective Ni amount (wt%) | 7.6 | | 7.4 | |
| Effective Ca amount (wt%) | 9.0 | | 8.2 | |
| Ni particle size by SEM (nm) | 4.5 | | 30 | |
| Ethanol conversion (%) | 100 | 94 | 100 | 100 |
| H ₂ yield (%) | 75 | 65 | 70 | 50 |
| H ₂ productivity (mol/min Kg _{cat}) | 2.4 | 2.2 | 2.2 | 1.8 |
| CO ₂ (%) - CO (%) | 30-12 | 25-6 | 31-12 | 31-3 |

Sustainable Energy and Fuels

ARTICLE

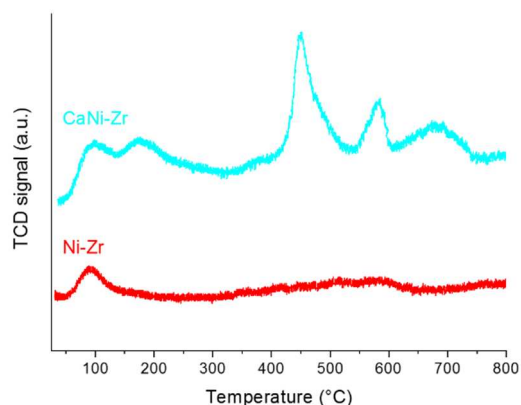
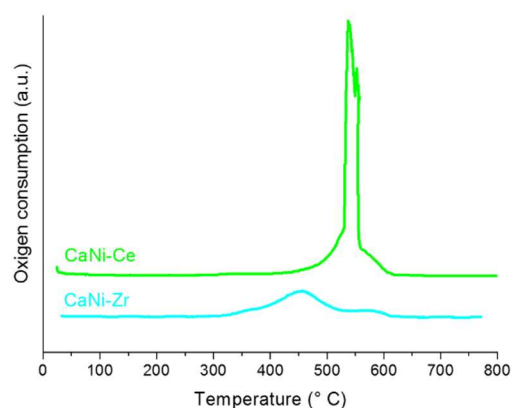
Figure 10: CO₂-TPD profiles of CaNi-Zr and Ni-Zr

Figure 10 shows CO₂-TPD of CaNi-Zr and Ni-Zr samples. For Ni-Zr catalyst only one peak is present at 100 °C while for CaNi-Zr there are multiple peaks between 100 °C and 700 °C. It's known that the nature of the sites is correlated with the temperature of the peaks: higher the temperature of the peak, stronger the basic strength. The presence of various peak in the CO₂-TPD of CaNi-Zr indicates that with the addition of calcium on the support, there is an increase of the number of strong basic sites. Therefore, the introduction of Ca on the support increases its basic properties, limits ethanol dehydrogenation and reduces carbon deactivation. In fact, the carbon balance is 20% higher for the calcium containing zirconium sample, less coke is deposited on the active sites and thus the activity is kept longer. The resistance towards coking increased due to the formation of oxygen vacancies, that can activate CO₂ and H₂O, thus favouring the gasification of coke.²¹ With the addition of calcium on ceria the carbon balance is slightly higher, but coke is still formed. This has been proven by TPO profiles of used catalysts (Figure 11). It is clear that coke is deposited on both sample. In contrast with the Ni-Zr and Ni-Ce samples, which had a single peak at the same temperature, these two catalysts present peaks at different temperatures. For CaNi-Ce, no shift in peak position has been observed. In the case CaNi-Zr, the oxidation peak is shifted towards lower temperatures indicating a higher oxidability of carbon species. This could explain the higher activity of CaNi-Zr compared to Ni-Zr sample.

Figure 11: TPO profiles CaNi-Zr and CaNi-Ce

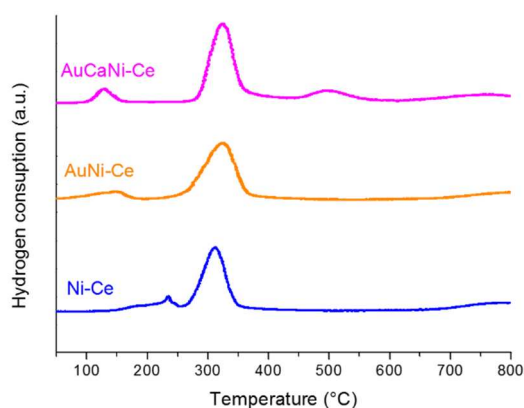


3.3 Promotion with Gold

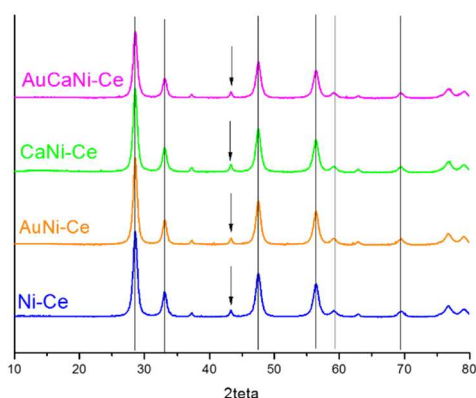
From the previous experiments, ceria was selected as support for its consistency throughout the reaction. The main problem, the deactivation of Ni-Ce could not be entirely prevented through the addition of calcium oxide in order to make it more basic and prevent coke formation. To improve total hydrogen production we have decided to add gold nanoparticles. As mentioned in the introduction, gold is known for its activity in water-gas shift reaction. Adding gold thus could lead to a higher hydrogen productivity. Moreover, the addition of calcium oxide in combination with gold was performed.

TPR were carried out in order to study the reducibility of the materials, which is related to the Ni and Au activation (Figure 12). The profiles of both gold promoted samples show a small reduction peak at 100 °C, which can be ascribed to the deposited gold nanoparticles.^{38, 39}

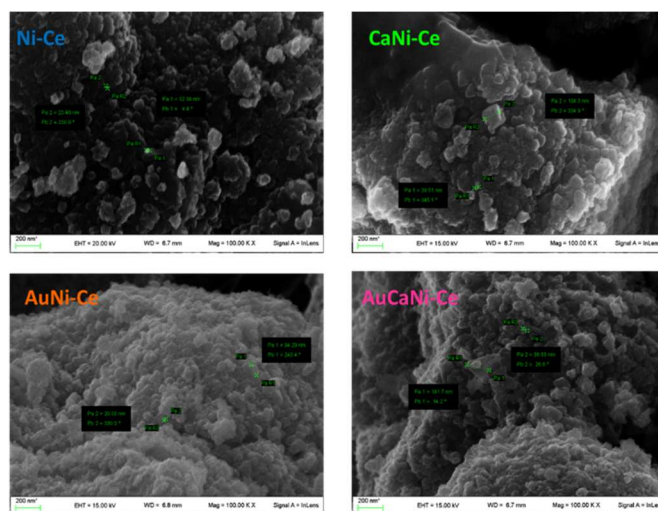
The peak ascribed to nickel reduction is still centred at 300 °C. Thus, all metals are reduced before reaching the reaction temperature (500 °C). For AuCaNi-Ce, a peak at 480 °C is noticed, which corresponds to the reduction peak of calcium oxide.

Figure 12: TPR profiles of all cerium oxide based catalysts

The structure of the four ceria supported samples was investigated by X-ray diffraction and the obtained patterns are shown in Figure 13 in the 2θ region between 10 and 80°. The peaks observed at $2\theta = 28, 33.5, 47.5, 56, 59,$ and 69° can be assigned to (111), (200), (220), (311), (222), and (400) peaks, respectively, of cubic CeO_2 (ceria, cerianite-(Ce), syn; file number 00-034-0394). The occurrence of NiO is clearly detected at $2\theta 43.4^\circ$. The analysis by Scherrer indicates a mean metal particle size of 23, 25, 25, 26 nm respectively for Ni-Ce, AuNi-Ce, CaNi-Ce, AuCaNi-Ce. The size of the active phase is therefore very similar for the four samples. The expected diffraction peaks associated with the presence of crystalline gold should appear at $38.1, 44.3, 64.5, 77.6,$ and 81.6° , corresponding to the (111), (200), (220), (311), and (222) faces of the cubic structure [file number 4-0784]. However, no peaks ascribable to crystalline Au have been detected for the two catalysts. This absence might be related to the low amount of Au (1 wt %) and to the presence of highly dispersed gold nanoparticles on ceria, not detectable by XRD.

Figure 13: XRD profiles of ceria based samples

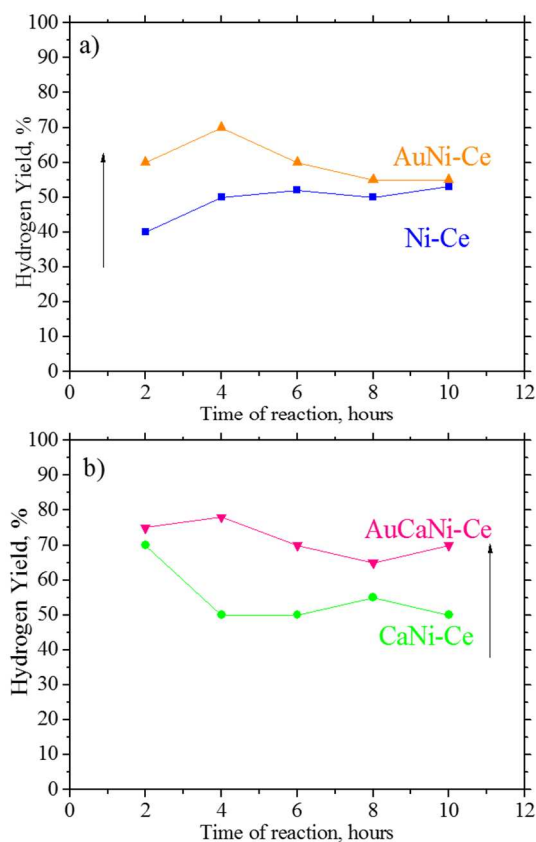
SEM analyses of ceria based catalysts are reported in Figure 14. For the four samples there is evidence of nickel nanoparticles with a size in the range 20-40 nm, in agreement with XRD results previously discussed. Moreover, on all the samples, cubic nanoparticles of ceria (60-100nm) are evident. EDX analyses indicate that nickel is well homogeneously distributed on the ceria support. EDX results have shown that also gold is homogeneous on the support of ceria for both AuNi-Ce and AuCaNi-Ce. Gold nanoparticles are hardly detectable due to the very low Au amount; only few triangular formations associated to Au (111) nanoparticles⁴⁰ were found, as shown in Figure 14.

Figure 14: SEM images of ceria based samples

As for ESR, for all cerium oxide based samples, the ethanol conversion was still complete after 10 hours of reaction. The most noteworthy effect of gold addition is the increase of hydrogen yield, as shown in Figure 15.

Although the yield went up, the selectivity towards CO was decreased, meaning that the water gas shift reaction was promoted during the catalytic activity. The catalytic performances in general increased, meaning that the gold nanoparticles in combination with the nickel are able to break more C-H bonds than nickel alone. The overall increase in productivity was measured at $0,6 \text{ mol}/(\text{min} \cdot \text{kg}_{\text{catalyst}})$. This proves that gold nanoparticles improve hydrogen production from ethanol on a Ni-Ce system. As shown in Figure 15, this is true for gold addition on both Ni-Ce and CaNi-Ce. Best performing catalyst is AuCaNi-Ce, where the basic doping of CaO and the promotion of the WGS by gold nanoparticles contribute to the highest yield.

Figure 15: Hydrogen yield for cerium based catalysts: Ni-Ce, AuNi-Ce (section a), CaNi-Ce and AuCaNi-Ce (section b).



4. Conclusions

The support plays a very important role on nickel activity in ESR. Zirconium and cerium oxides proved to be suitable supports, even if both still suffer from coking phenomena. Calcium addition allowed for both a substantial increase in hydrogen productivity and yield. The resistance towards coking increased due to the formation of oxygen vacancies, that can activate CO₂ and H₂O, thus favouring the gasification of coke. Overall seen the addition of calcium is preventing the deactivation, in particular for zirconia based catalyst.

Gold nanoparticles on cerium oxide by deposition precipitation greatly improved hydrogen production. Doping with both calcium oxide and gold nanoparticles led to the best performing catalyst. In fact, the basic doping by CaO and the promotion of the WGS by gold nanoparticles contributed to the highest hydrogen production.

5. References

- O.Y. Edelenbosch, K. Kermeli, W. Crijns-Graus, E. Worrell, R. Bibas, B. Fais, S. Fujimori, P. Kyle, F. Sano, D.P. van Vuuren, *Energy* 2017, **122**, 701-710.

- <http://www.bp.com/en/global/corporate/investors/results-and-reporting/annual-report.html>.
- Y. D. Goswami, F. Kreith, *Energy efficiency and renewable energy handbook*, second edition, CRC press, London, 2015.
- J. Matthey, *Fuel Cell Electric Vehicles: the road ahead*, www.fuelcelltoday.com, Poyston, UK, 2013.
- P. McKendry, *Bioresource Technology*, 2002, **83**, 37-46.
- A. Le Valant, F. Can, N. Bion, D. Duprez, F. Epron, *Int. J. Hydrogen Energy*, 2010, **35**, 5015-5020.
- M.H. Youn, J.G. Seo, H. Lee, Y. Bang, J.S. Chung, I.K. Song, *Appl. Catal. B*, 2010, **98**, 57-64.
- G. Wen, Y. Xu, H. Ma, Z. Xu, Z. Tian, *Int. J. Hydrogen Energy*, 2008, **33**, 6657-6666.
- S. Cavallaro, N. Mondello, S. Freni, *J. Power Sources*, 2001, **102**, 198-204.
- A.J. Vizcaíno, A. Carrero, J.A. Calles, *Int. J. Hydrogen Energy*, 2007, **32**, 1450-1461.
- J. Y. Chiou, C.L. Lai, S. Yu, H. Huang, C. Chuang, C. Wang, *Int. J. Hydrogen Energy*, 2014, **39**, 20689-20699.
- J. P. Breen, R. Burch, H. M. Coleman, *Appl. Catal. B*, 2002, **39**, 65-74.
- S. Tosti, D. Lecci, C. Rizzello, A. Basile, Patent RM2006A000102, 2006.
- B. Nematollahi, M. Rezaei, E. N. Lay, *Chem. Eng. Technol.* 2015, **38**, 265-273.
- Q. Fu, S. Fiore, H. Saltsburg, X. Qi, *Fuel Chemistry Division Preprints*, 2002, **47** (2), 605-606.
- B. Nematollahi, M. Rezaei, E. N. Lay, *J. Rare Earths*, 2015, **33** 6, 619-628.
- W. Cai, F. Wang, E. Zhan, A.C. Van Veen, C. Mirodatos, W. Shen, *J. Catal.*, 2008, **257**, 96-107.
- A. Valentini, N. Carreno, L. Probst, A. Barison, A. Ferreira, E. Leite, E. Longo, *Appl. Catal. A*, 2006, **310**, 174-182.
- A. Norman, V. Perrichon, *Phys. Chem. Chem. Phys.*, 2003, **5**, 3557-3564.
- W. Hongjing, V. La Parola, *Catalysts*, 2013, **3**, 563-583.
- V. Nichele, M. Signoreto, F. Pinna, F. Menegazzo, I. Rossetti, G. Cruciani, G. Cerrato, A. Di Michele, *Appl. Catal. B*, 2014, **150-151**, 12-20.
- G. C. Bond, C. Louis, D. T. Thompson, *Catalysis by gold*, London: Imperial College Press, 2006.
- J. da Silva Lima Fonseca, H. S. Ferreira, N. Bion, L. Pirault-Roy, M. Do Carmo Rangel, D. Duprez, F. Epron, *Catal.Today*, 2012, **180**, 34-41.
- S. H. Oh, R. M. Sinkevitch, *J. Catal.*, 1993, **142**, 254-262.
- M. Signoreto, F. Menegazzo, V. Trevisan, F. Pinna, M. Manzoli, F. Boccuzzi, *Catalysts*, 2013, **3**, 656-670.
- T.R. Reina, S. Ivanova, M.A. Centeno, J.A. Odriozola, *Appl. Catal. B*, 2016, **187**, 98-107.
- J.L. Santos, T.R. Reina, S. Ivanova, M.A. Centeno, J.A. Odriozola, *Appl. Catal. B*, 2017, **201**, 310-317.
- S. He, L. Zhang, X. Li, J. Wang, D. He, J. Lu, Y. Luo, *Catal. Today*, 2015, **258**, 162-168.

- 29 V. Nichele, M. Signoretto, F. Menegazzo, I. Rossetti, G. Cruciani, *Int. J. Hydrogen Energy*, 2014, **39**, 4252-4258.
- 30 L. Kundakovic, M. Flytzani-Stephanopoulos, *J. Catal.*, 1998, **179**, 203-221.
- 31 S. Brunauer, P. H. Emmett, E. Teller, *JACS*, 1938, **60**, 309-319.
- 32 E. P. Barrett, L. S. Joyner, P. P. Halenda, *JACS*, 1951, **73**, 373-380.
- 33 A. Venugopal, J. Aluha, M. Scurrill, *Catal. Lett.* **90** (2003) 1-6.
- 34 L. Zhang, J. Lin, Y. Chen, *J. Chem. Soc. Faraday Trans.*, 1992, **88** (14), 2075-2078.
- 35 Y.Q. Song, D.H. He, B.Q. Xu, *Appl. Catal. A* **337** (2008) 19-28.
- 36 V. García, J.J. Fernández, W. Ruíz, F. Mondragón, A. Moreno, *Catal. Commun.*, 2009, **11**, 240-246.
- 37 J.D.A. Bellido, J.E. De Souza, J.C. M'Peko, E.M. Assaf, *Appl. Catal. A*, 2009, **358**, 215-223.
- 38 F. Ying, S. Wang, C.-T. Au, S.-Y. Lai, *Gold Bull.*, 2010, **43**, 241-251.
- 39 Q. Fu, A. Weber, M. Flytzani-Stephanopoulos, *Catal. Lett.*, 2001, **77**, 87-95.
- 40 M. Tréguer-Delapierre, J. Majimel, S. Mornet, E. Duguet, S. Ravaine, *Gold Bull.*, 2008, **41**, 195-207.